Testing star formation laws in a starburst galaxy at redshift 3 resolved with ALMA

P. Sharda,[1,2,3]★ C. Federrath,[4]★ E. da Cunha,[4] A. M. Swinbank[5,6] and S. Dye[7]

[1]*Department of Physics, Birla Institute of Technology and Science, Pilani, Rajasthan 333031, India*
[2]*Department of Electrical and Electronics Engineering, Birla Institute of Technology and Science, Pilani, Rajasthan 333031, India*
[3]*Department of Physics and Astronomy, University of Exeter, Stoker Road, Exeter EX4 4QL, UK*
[4]*Research School of Astronomy and Astrophysics, The Australian National University, Canberra, ACT 2611, Australia*
[5]*Institute for Computational Cosmology, Durham University, Durham DH1 3LE, UK*
[6]*Centre for Extragalactic Astronomy, Department of Physics, Durham University, Durham DH1 3LE, UK*
[7]*School of Physics and Astronomy, University of Nottingham, University Park, Nottingham NG7 2RD, UK*

ABSTRACT

Using high-resolution (sub-kiloparsec scale) data obtained by ALMA, we analyse the star formation rate (SFR), gas content, and kinematics in SDP 81, a gravitationally lensed starburst galaxy at redshift 3. We estimate the SFR surface density (Σ_{SFR}) in the brightest clump of this galaxy to be $357^{+135}_{-85}\,M_\odot\,\mathrm{yr}^{-1}\,\mathrm{kpc}^{-2}$, over an area of $0.07 \pm 0.02\,\mathrm{kpc}^2$. Using the intensity-weighted velocity of $CO\,(5\text{--}4)$, we measure the turbulent velocity dispersion in the plane of the sky and find $\sigma_{v,\,turb} = 37 \pm 5\,\mathrm{km\,s}^{-1}$ for the clump, in good agreement with previous estimates along the line of sight. Our measurements of the gas surface density, freefall time, and turbulent Mach number allow us to compare the theoretical SFR from various star formation models with that observed, revealing that the role of turbulence is crucial to explaining the observed SFR in this clump. While the Kennicutt–Schmidt (KS) relation predicts an SFR surface density of $\Sigma_{SFR,\,KS} = 52 \pm 17\,M_\odot\,\mathrm{yr}^{-1}\,\mathrm{kpc}^{-2}$, the single-freefall model by Krumholz, Dekel, and McKee (KDM) predicts $\Sigma_{SFR,\,KDM} = 106 \pm 37\,M_\odot\,\mathrm{yr}^{-1}\,\mathrm{kpc}^{-2}$. In contrast, the multifreefall (turbulence) model by Salim, Federrath, and Kewley (SFK) gives $\Sigma_{SFR,SFK} = 491^{+139}_{-194}\,M_\odot\,\mathrm{yr}^{-1}\,\mathrm{kpc}^{-2}$. Although the SFK relation overestimates the SFR in this clump (possibly due to the negligence of magnetic fields), it provides the best prediction among the available models. Finally, we compare the star formation and gas properties of this galaxy to local star-forming regions and find that the SFK relation provides the best estimates of SFR in both local and high-redshift galaxies.

Key words: Turbulence – Stars: formation – galaxies: high-redshift – galaxies: starburst – Galaxy: kinematics and dynamics – Submillimetre: galaxies.

1 INTRODUCTION

Numerous star formation relations have been proposed in a quest to universalize the theory of star formation, by linking the star formation rate (SFR) with the mass of gas, its freefall time, virial parameter, magnetic field strength, and turbulence (Silk 1997; Kennicutt 1998a; Elmegreen 2002; Shi et al. 2011; Krumholz, Dekel & McKee 2012 (hereafter, KDM12); Renaud, Kraljic & Bournaud 2012; Elmegreen 2015; Elmegreen & Hunter 2015; Escala 2015; Salim, Federrath & Kewley 2015 (hereafter, SFK15); Nguyen-Luong et al. 2016; Miettinen et al. 2017). While these relations have been shown

to be valid for star-forming regions in the Milky Way and local galaxies (Bigiel et al. 2008), the lack of spatial resolution has limited us in testing them on high-redshift sources with $z > 1$. Thanks to the high spatial resolution of ALMA, several high-redshift galaxies emitting in the submillimetre (sub-mm) regime have been detected and resolved over the last few years (Decarli et al. 2016; Spilker et al. 2016; Brisbin et al. 2017; Danielson et al. 2017; Lu et al. 2017), particularly if they are gravitationally lensed by a foreground source (Smail, Ivison & Blain 1997; Smail et al. 2002; Hezaveh et al. 2013; Bradač et al. 2017; Fudamoto et al. 2017; Johnson et al. 2017; Laporte et al. 2017; Wong et al. 2017). These galaxies are known to be rigorous sites of dusty star formation where molecular gas plays a key role in modifying the structure of clusters where star formation occurs. Tracing molecular gas in these regions can give us valuable insight on the star formation characteristics of these galaxies since

★ E-mail: piyush.suneet@gmail.com (PS); christoph.federrath@anu.edu.au (CF)

it is believed that molecular gas has a strong correlation with SFR whereas atomic gas does not (Wong & Blitz 2002; Bigiel et al. 2008; Blanc et al. 2009).

J090311.6+003906 (hereafter, referred to as SDP 81) was detected as a lensed galaxy in the *H-ATLAS* survey of bright submillimetre galaxies (SMGs) by Negrello et al. (2010), where the redshift was measured as $z = 3.042 \pm 0.001$ through ground-based CO measurements. It falls in the popular definition of SMGs where the 850 μm flux density $S_{850} > 3$ mJy and infrared luminosity $L_{IR} \gtrsim 10^{12} \, L_{\odot}$ (Kovács et al. 2006; Coppin et al. 2008; Hayward et al. 2011). SDP 81 has also been established to be a dusty star-forming galaxy in previous works (Negrello et al. 2014; Swinbank et al. 2015 (hereafter, S15); Dye et al. 2015; Hatsukade et al. 2015; Rybak et al. 2015a,b; Tamura et al. 2015; Wong, Suyu & Matsushita 2015; Hezaveh et al. 2016; Inoue et al. 2016). Even though there are significant uncertainties in determining the stellar mass of SDP 81, we note that it lies 1–2 orders of magnitude above the main sequence on the stellar mass−star formation rate ($M_{\star}$−SFR) plane (Speagle et al. 2014; Chang et al. 2015; Guo et al. 2015; Schreiber et al. 2015). Thus, SDP 81 falls under the category of extreme starburst galaxies and is an ideal candidate to test star formation relations. This is further confirmed by the position of SDP 81 on the star formation rate−gas mass (SFR − M_{gas}) plane (Sargent et al. 2014).

Our goal in this work is to extract the SFR in individual *clumps* of this galaxy and compare it with that predicted by existing star formation relations. We refer to clumps as giant star-forming regions (Genzel et al. 2006; Elmegreen et al. 2009; Bournaud et al. 2014) substantially more massive and star-forming than typical molecular clouds in the Milky Way (Cowie, Hu & Songaila 1995; Van den Bergh et al. 1996; Shapiro, Genzel & Förster Schreiber 2010), and possibly showing high star formation efficiencies (Freundlich et al. 2013; Zanella et al. 2015; Cibinel et al. 2017). The paper is organized as follows: in Section 2, we summarize the data reduction through lens modelling which was used to create the source plane reconstructed images of SDP 81 (Dye et al. 2015). This section also identifies different clumps extracted in this galaxy by S15. Section 3 entails the dust spectral energy distribution (SED) fitting of a modified blackbody (MBB) and estimation of SFR surface density in the galaxy. We describe the kinematic analysis of CO (5–4) used to estimate the Mach number in Section 4. In Section 5, we present our estimates of the local gas mass and freefall time in the galaxy. Finally, we put all these parameters together to test various star formation relations and compare with the SFR surface density deduced through dust SED fitting, in Section 6. We summarize our findings in Section 7.

We adopt the ΛCDM cosmology with $H_0 = 72 \, \mathrm{km \, s^{-1} \, Mpc^{-1}}$, $\Omega_m = 0.27$, $\Omega_{\Lambda} = 1 - \Omega_m$ and the Chabrier IMF (Chabrier 2003). The luminosity distance and scale length corresponding to these parameters is 25.9 Gpc and 7.69 kpc arcsec^{-1}, respectively, for $z \approx 3.042$ (Wright 2006).

2 DATA REDUCTION AND ANALYSIS

ALMA observations of SDP 81 (RA = $09^h03^m11.57^s$, Dec. = +00°39′06.6″) were taken during the Science Verification cycle in 2014 October. In the calibrated data, the lensed galaxy is seen in the form of an Einstein ring, with two arcs on the eastern and western sides (Dye et al. 2014; ALMA Partnership 2015). Through uv tapering, a resolution of ∼150 × 120 mas was achieved in the three bands (see tables 1 and 3 of ALMA Partnership (2015) for observed fluxes and noise levels). The CO (5–4) velocity cubes were binned to a velocity resolution of 21 km s^{-1} (ALMA Partnership 2015).
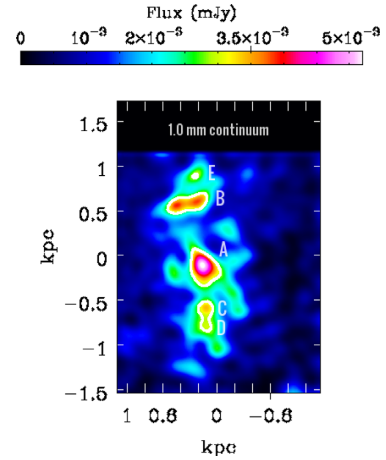
Figure 1. Source reconstructed image of continuum flux in ALMA band 7 ($\lambda_{obs} = 1.0$ mm), created using CASA (McMullin et al. 2007). The contours depict clumps A, B, C, D, and E, taken from fig. 1 of S15. We do not use clumps B, C, D, and E in this work because they do not allow for accurate estimates of kinematics and volume densities from the plane-of-the-sky projection.

We use the source plane reconstructed images of continuum emission (in ALMA bands 4, 6, and 7, corresponding to $\lambda_{obs} = 2.0$, 1.3, and 1.0 mm, respectively) and CO (5–4) flux and velocity, created by S15, using the lensing model by Dye et al. (2015). This model was used in the image plane with the semilinear inversion method (Warren & Dye 2003) developed by Nightingale & Dye (2015). The average luminosity-weighted magnification factors derived by Dye et al. (2015) for the continuum in bands 6 and 7 are 15.8 ± 0.7 and 16.0 ± 0.7, respectively. This magnification is representative of a higher resolution by a factor of ∼30 (sub-kpc scale) than that in the typical non-lensed case (Ikarashi et al. 2015; Simpson et al. 2015).

S15 identified five molecular clumps from the continuum emission maps where intense star formation is taking place (see fig. 1 in their paper), using a signal to *local* noise (SNR) cutoff at 5σ. Of these clumps, only clumps A and B have sufficient resolution (number of pixels) to perform the kinematic analysis to estimate the turbulent velocity dispersion (see Fig. 1). The horizontally elongated structure of clump B rules out the possibility of a spherical approximation to its volume which we otherwise cannot estimate, not to mention that its location does not correlate well with the CO (5–4) flux map. Clump A, on the other hand, has a strong correlation with CO (5–4) flux and appears symmetric, as seen in Fig. 1. Hence, we restrict our analysis to clump A in this work. We notice that clump A likely coincides with the centre of the galaxy and might be its nucleus/forming core. Thus, it might be significantly different in origin from clumps residing in the outer regions of the disc.

3 MEASUREMENT OF THE STAR FORMATION RATE

We estimate the SFR surface density (Σ_{SFR}) in clump A by fitting a modified blackbody (MBB) spectrum to the continuum emission from dust in the three ALMA bands. The MBB spectral law can be written as

$$S_{\nu} = N_{\nu} \left(\frac{2h\nu^3}{c^2} \right) \frac{1}{e^{h\nu/k_B T} - 1} \, \nu^{\beta_{em}}, \tag{1}$$

where ν is the rest-frame frequency, S_ν is the flux density of the clump, N_ν is the normalization parameter (includes dust opacity), T is the dust temperature, and β_{em} is the emissivity index ($\beta_{em} = 0$ corresponds to a blackbody) (Draine & Lee 1984; Da Cunha et al. 2010b). Since clump A lies near the centre of the galaxy where the background contribution may be high, we subtract the underlying (disc) CO emission from clump A by masking the clump and then smoothing the image by convolving it with a large Gaussian kernel. Then, we subtract the smoothed image from the original image to get the background subtracted image. In order to ensure that we do not over or undersubtract, we reiterate this procedure multiple times with different kernels.

The flux density can be integrated over the whole infrared (IR) range (8–1000 μm) to get the dust luminosity (Humason, Mayall & Sandage 1956; Oke & Sandage 1968; Hogg et al. 2002):

$$L_{FIR} = \frac{4\pi D_L^2}{1+z} \int_{8\,\mu m}^{1000\,\mu m} S_\nu \, d\nu, \qquad (2)$$

where L_{FIR} is the far-infrared luminosity of the clump, D_L is the luminosity distance to SDP 81 and S_ν is the flux density of the clump. However, the available ALMA observations are insufficient to simultaneously constrain the dust parameters – T, β_{em}, and L_{FIR}. Therefore, we fix $\beta_{em} = 1.5$, 2.0, and 2.5, which are the typically used values for starburst galaxies (Hildebrand 1983; Blain, Barnard & Chapman 2003; Casey 2012; Smith et al. 2013). We also include observed fluxes at various other wavelengths in the infrared regime, reported in table 2 of Negrello et al. (2014), which cover a longer wavelength baseline ($\lambda_{obs} = 350$–2000 mm). Then, using a two-step fitting process: (1) we fit the galaxy-integrated fluxes to constrain T and β_{em} and (2) we then adopt the 'galaxy-wide' T and β_{em} to fit clump A and determine its far-infrared luminosity. The conditions of individual clumps might be very different as compared to the whole galaxy. We lack the spatial resolution for a proper decomposition of the various clumps and assume that the clump conditions (of clump A) are identical to the galaxy-wide properties, while being aware that this might not be the case. We include the systematic uncertainty arising from this assumption in our calculation of the far-infrared luminosity.

We derive a best-fitting temperature $T = 39 \pm 2$ K for $\beta_{em} = 2.5$, where we use Monte Carlo (MC) simulations (by modelling the uncertainties in the observed fluxes according to a Gaussian distribution) to find the best-fitting MBB (Ogilvie 1984; Johnson et al. 2013). The uncertainty on T arises from the inclusion of the flux at 350 μm (from SPIRE observations, Griffin et al. 2010) which falls partially under the cold temperature dominated regime (see fig. 6 of Dye et al. 2015). Fig. 2 shows the best-fitting MBB we find for clump A from the fits, along with the $1\,\sigma$ uncertainty range we derive from the $1\,\sigma$ uncertainty of the far-infrared luminosity (L_{FIR}) obtained using MC error propagation.

We obtain nearly identical values of (T, β_{em}) from the two fitting methods we use: pixel-by-pixel and whole clump. In the pixel-by-pixel algorithm, we find the SFR in each pixel by fitting the MBB using the best-fitting (T, β_{em}) values. Then, we sum the SFRs from each pixel to get SFR for the whole clump. On the contrary, in the whole clump fitting algorithm, we first sum the fluxes from each pixel and then find the SFR by fitting the MBB using the best-fitting (T, β_{em}) values. The SFRs we obtain from both the methods agree well with each other, within ±3 per cent.

Using equation (2), we derive $L_{FIR} = \left(2.25^{+0.95}_{-0.47}\right) \times 10^{11}$ L$_\odot$ for clump A, where the uncertainty includes statistical as well as systematic errors. The observed SFR surface density we find using the L_{FIR}–SFR relation from Kennicutt (1998a) is $\Sigma_{SFR} = $
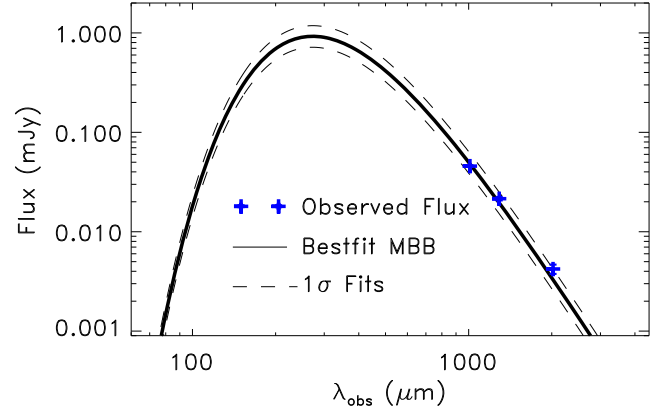
Figure 2. SED fit applied to clump A with $T = 39$ K, $\beta_{em} = 2.5$ [parameters obtained from SED fit of data from SPIRE (Griffin et al. 2010), SMA (Bussmann et al. 2013), MAMBO (Negrello et al. 2010), and ALMA (ALMA Partnership 2015)]. Observed fluxes for the three ALMA bands are shown in blue. Dashed lines indicate the $1\,\sigma$ uncertainty range of the fit.

555^{+197}_{-120} M$_\odot$ yr^{-1} kpc^{-2}. Since this relation uses a Salpeter IMF (Salpeter 1955), we adjust its coefficient by a factor of 1.6 downward to adapt to 'the Chabrier IMF' (Chabrier 2003) to be consistent throughout our work (Da Cunha et al. 2010a,b). The resulting SFR surface density we get is $\Sigma_{SFR} = 357^{+135}_{-85}$ M$_\odot$ yr^{-1} kpc^{-2}. These values are representative of intense star formation and are expected for the central regions of high-redshift starburst galaxies (Cañameras et al. 2017; Cibinel et al. 2017).

To reinforce our estimation of flux densities in the three ALMA bands as obtained after background subtraction, we also model the fluxes using an n-Sérsic profile ($R^{1/n}$) for the disc, with a Gaussian added to it for clump A (Sersic 1968; Caon, Capaccioli & D'Onofrio 1993; Ciotti & Bertin 1999; Trujillo, Graham & Caon 2001; Aceves, Velázquez & Cruz 2006). The Sérsic index (n) we obtain for $\lambda_{obs} = 1.0$ mm continuum is $n \sim 0.5$. Although our result is lower than the average median value reported in Hodge et al. 2016 ($n \approx 1 \pm 0.2$, see also Paulino-Afonso et al. 2018), it is consistent with the Sérsic indices found in several high-redshift galaxies (see table 1 of Hodge et al. 2016). Through this composite profile, the fluxes we obtain for clump A for the three bands are similar to those obtained through background subtraction discussed above, within ±12 per cent. Since this difference in flux densities is negligible, the resulting L_{FIR} and Σ_{SFR} from this method are similar to those we quoted above, within the uncertainties.

3.1 Gas mass and clump size from continuum emission

Apart from the SFR surface density, we can also estimate the gas mass (M_{gas}) and size of the clump (R) using the SED fits and continuum maps, respectively. Since we have an excellent coverage of the Rayleigh–Jeans regime, we use our best-fitting MBB to estimate the dust mass of clump A by using equation 6 of Magdis et al. (2012) and appropriate rest-frame dust mass absorption coefficients for the three ALMA bands, from table 6 of Li & Draine (2001). Then, we use a typical gas-to-dust conversion ratio of 150 to get the gas mass in this clump (Dunne et al. 2000; Dye et al. 2015; Brisbin et al. 2017). For the three ALMA bands, the gas masses we thereby obtain are $M_{gas} = (2.3$–4.9$) \times 10^8$ M$_\odot$. This is consistent with the value of M_{gas} we obtain from CO (5–4) (as we discuss in detail in Section 5).

Table 1. Results for Clump A in SDP 81 (see Fig. 1) with mean and 1σ errors.

Parameter	Value
β_{em}	2.5
T	39 ± 2 K
L_{FIR}	$(2.3^{+1.0}_{-0.5}) \times 10^{11}$ L$_\odot$
Σ_{SFR} (observed)[a]	357^{+135}_{-85} M$_\odot$ yr^{-1} kpc^{-2}
A	$(7.2 \pm 1.5) \times 10^{-2}$ kpc^2
R	$(1.5 \pm 0.2) \times 10^{-1}$ kpc
$\sigma_{v,bgs}$[b]	80 ± 10 km s^{-1}
$\sigma_{v,turb}$[c]	37 ± 5 km s^{-1}
c_s	0.4 ± 0.2 km s^{-1}
$\mathcal{M}$	96 ± 28
b	0.4
$S_{v,CO(5-4)}v$[d]	8.4 ± 1.8 mJy km s^{-1}
$L'_{CO(1-0)}$	$(1.4 \pm 0.1) \times 10^8$ K km s^{-1} pc^2
r_{54}	0.28 ± 0.05
$L'_{CO(5-4)}$	$(5.0 \pm 1.1) \times 10^8$ K km s^{-1} pc^2
α_{CO}	0.9 ± 0.2 M$_\odot$ (K km s^{-1} pc^2)$^{-1}$
M_{gas}	$(6.2 \pm 1.4) \times 10^8$ M$_\odot$
Σ_{gas}	$(8.6 \pm 1.9) \times 10^9$ M$_\odot$ kpc^{-2}
ρ	$(2.9 \pm 0.6) \times 10^{-21}$ g cm^{-3}
α_{vir}	0.6 ± 0.1
t_{ff}	$(1.3 \pm 0.1) \times 10^6$ yr
Σ_{SFR} (K98)[a, e]	52 ± 17 M$_\odot$ yr^{-1} kpc^{-2}
Σ_{SFR} (KDM12)[f]	106 ± 37 M$_\odot$ yr^{-1} kpc^{-2}
Σ_{SFR} (SFK15)[g]	491^{+139}_{-194} M$_\odot$ yr^{-1} kpc^{-2}

[a]Corrected for Chabrier IMF.

[b]Large-scale velocity dispersion before gradient subtraction.

[c]Turbulent velocity dispersion after gradient subtraction.

[d]Integrated CO (5–4) flux after background subtraction.

[e]16th and 84th percentiles are 37 and 64 M$_\odot$ yr^{-1} kpc^{-2}.

[f]16th and 84th percentiles are 74 and 132 M$_\odot$ yr^{-1} kpc^{-2}.

[g] Errors represent the 16th and 84th percentiles.

We use the composite disc profile (n-Sérsic disc + Gaussian clump, as discussed in Section 3) to find an estimate of the size of clump A. Since the clump is defined using the $\lambda_{obs} = 1.0$ mm continuum obtained from ALMA, we use the best-fitting composite disc profile at this wavelength and find the size of this clump by assuming that its diameter is equal to the full width at half-maximum of the composite profile (i.e. FWHM $= 2R$). Correspondingly, we obtain $R \sim 0.16$ kpc for clump A. This is in good agreement with the size of clump A we find in Section 5 by summing up the pixels belonging to clump A, as we report in Table 1.

4 MACH NUMBER ESTIMATION

Supersonic turbulence is a key ingredient to star formation because it can compress interstellar gas which leads to the formation of dense cores. On the other hand, it can suppress the global collapse of the clouds, thus significantly reducing the SFR (Elmegreen & Scalo 2004; Mac Low & Klessen 2004; McKee & Ostriker 2007; Hennebelle & Falgarone 2012). The root mean square sonic Mach number associated with turbulence in star-forming regions is given by

$$\mathcal{M} = \frac{\sigma_{v,turb}}{c_s}, \qquad (3)$$

where $\sigma_{v,turb}$ is the turbulent velocity dispersion and c_s is the sound speed. $c_s \propto \sqrt{T}$, where T is the gas temperature. It is difficult to estimate the gas temperature with the current data, however, we can assume it to be between 10 and 100 K. This assumption is valid

for gas temperatures in dense molecular clouds (Gao & Solomon 2004; Solomon & Vanden Bout 2005; Wu et al. 2005; Battersby et al. 2014; Immer et al. 2016; Krieger et al. 2017). Using the relation for isothermal sound speed from Federrath et al. (2016) for a mean molecular weight of 2.33 (Kauffmann et al. 2008) and $T_{gas} \approx 10$ K, the sound speed is ~ 0.2 km s^{-1}, whereas it is ~ 0.6 km s^{-1} for $T_{gas} \approx 100$ K; so we assume the sound speed to be in the range 0.2–0.6 km s^{-1}.

The CO (5–4) velocity map after source plane reconstruction shows a clear, large-scale gradient running diagonally, as we show in Fig. 3 (also, fig. 1 of S15). This systematic gradient can be associated with the rotational or shear motion of the gas. To extract the small-scale turbulent features in this clump, we fit a large-scale gradient to the clump and subtract it; similar to the analysis of turbulent velocity dispersion done on the central molecular zone (CMZ) cloud Brick by Federrath et al. (2016). For this purpose, we use the PLANEFIT routine in IDL which performs a least-squares fit of a plane to a set of (x, y, z) points. In this case, this set is a position–position–velocity (PPV) cube with x and y being the position coordinates of pixels forming clump A, and z being the CO (5–4) velocity of each pixel. We use the standard deviation of residuals after gradient subtraction as the turbulent velocity dispersion:

$$\sigma_{v,turb} = \sqrt{\frac{1}{N-1} \sum_{i=1}^{N} \left((v^i_{bgs} - v_{fg}) - \mu \right)^2}, \qquad (4)$$

where N is the number of pixels or resolution elements, v^i_{bgs} is the CO (5-4) velocity of the ith pixel before gradient subtraction, v_{fg} is the velocity of the fitted gradient and μ is the mean of residuals after gradient subtraction (i.e. $\mu = \langle (v^i_{bgs} - v_{fg}) \rangle$).

The turbulent velocity before subtracting the gradient is $\sigma_{v,bgs} = 80 \pm 10$ km s^{-1}. From the gradient subtraction algorithm, we obtain the turbulent velocity dispersion in clump A as $\sigma_{v,turb} = 37 \pm 5$ km s^{-1}, where the 1σ error is the standard deviation calculated using (Lehmann & Casella 1998):

$$s_{\sigma_v} = \sigma_v \cdot \frac{\Gamma\left(\frac{N-1}{2}\right)}{\Gamma(N/2)} \cdot \sqrt{\frac{N-1}{2} - \left(\frac{\Gamma(N/2)}{\Gamma\left(\frac{N-1}{2}\right)}\right)^2}, \qquad (5)$$

where $\Gamma(N)$ is the Gamma function. We also find the uncertainty on $\sigma_{v,turb}$ through MC simulations and note that the result is consistent with the value we obtain from the analytical equation, within ± 8 per cent. Fig. 3 shows the velocity field across clump A before gradient subtraction, fitted gradient velocities, and velocity field after gradient subtraction. By construction, the residuals after gradient subtraction are evenly spread around 0, as is also clear from the PDF of $\sigma_{v,turb}$ we plot in Fig. 4. From Fig. 4, we note that the distribution of velocities (in the pixels of clump A) before gradient subtraction is highly non-Gaussian and bimodal, while that of the velocities after gradient subtraction is more consistent with a Gaussian distribution. However, due to low-number statistics, it is hard to infer much information from this distribution; some non-Gaussian contributions may still remain after gradient subtraction, because it only removes the largest scale mode of systematic shear or rotation. None the less, this distribution is in agreement with velocity PDFs obtained for simulations of supersonic turbulence which are also Gaussian in nature (Klessen 2000; Federrath 2013) and the non-Gaussian components can arise from small-scale rotational or shear modes, or due to the intrinsic features of turbulence (see section 3.2.2 of Federrath et al. (2016) and references therein). Additionally, we note that the width of the Gaussian we fit for the PDF of
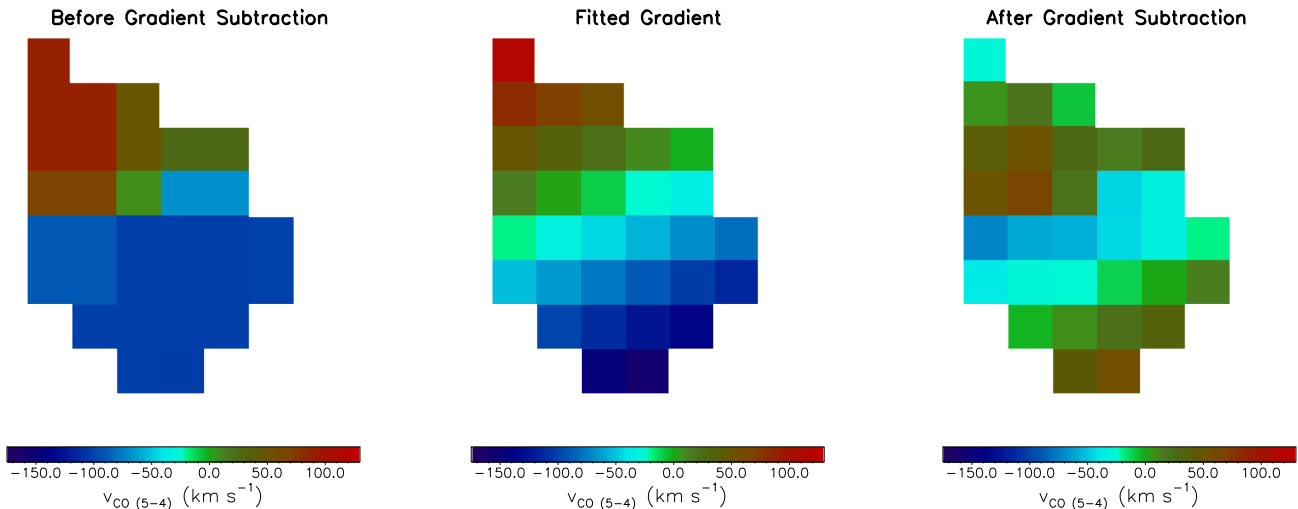
Figure 3. *Left-hand panel:* Centroid CO (5–4) velocity (in $km\,s^{-1}$) in the pixels of clump A before gradient subtraction. The size of each pixel is $\sim0.05\,kpc$. *Middle panel:* Fitted large-scale gradient to the clump. *Right-hand panel:* Velocity of CO (5–4) in the clump after gradient subtraction. The last panel isolates the turbulent velocities in the plane of the sky. The turbulent velocity dispersion obtained for clump A is $\sigma_{v,\,turb} = 37 \pm 5\,km\,s^{-1}$, using which the Mach number calculated is $\mathcal{M} = \sigma_{v,\,turb}/c_s = 96 \pm 28$.
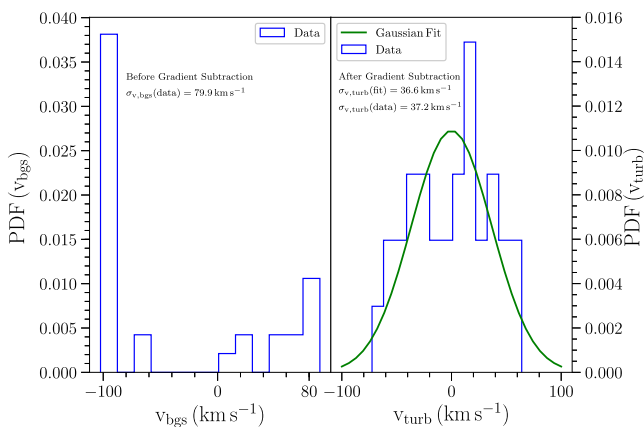
Figure 4. PDFs of CO (5–4) velocities of the pixels in clump A before and after gradient subtraction. The distribution of velocities before gradient subtraction (v_{bgs}) is bimodal; that of velocities after gradient subtraction (v_{turb}) resembles a Gaussian distribution, however, much information cannot be ascertained due to low number of statistics. The width of the Gaussian we fit (right-hand panel) and the data are similar, thus reinforcing the estimate of turbulent velocity dispersion $\sigma_{v,\,turb} = 37 \pm 5\,km\,s^{-1}$.

velocities after gradient subtraction matches well with what we find using the data (i.e. $\sigma_{v,\,turb}(\text{fit}) \approx \sigma_{v,\,turb}(\text{data})$).

The turbulent velocity dispersion we calculate is in agreement with the velocity dispersion of $30 \pm 9\,km\,s^{-1}$ calculated by S15 for this clump using the second moment map (i.e. the dispersion along the line of sight, after correction for beam smearing). The velocity dispersion we calculate is in the plane of the sky. A consensus between velocity dispersions using the two methods imply that clump A can be considered isotropic and it might be fair to approximate it as a sphere.

Using this turbulent velocity dispersion, we obtain a turbulent Mach number $\mathcal{M} = 96 \pm 28$. Although this is quite high compared to nearby galaxies (see Kennicutt & Evans (2012) and references therein), it falls in the range of Mach numbers associated with starburst galaxies (Gao & Solomon 2004; Bouché et al. 2007; Cresci

et al. 2009; Förster Schreiber et al. 2009; Tacconi et al. 2010). Given the high redshift of SDP 81 and previous works highlighting intense star formation, it is not unusual to obtain Mach numbers near 100. In fact, it implies that the role of turbulence becomes more important at the epoch near the maximum star formation in the history of the Universe (Springel & Hernquist 2003; Madau & Dickinson 2014; Falgarone et al. 2017).

4.1 Resolution check for gradient fit and subtraction algorithm

The gradient fit and subtraction algorithm works accurately only if the resolution is sufficient. For the CMZ cloud Brick, the resolution scale was in sub-parsecs (Federrath et al. 2016) whereas it is in sub-kiloparsecs for SDP 81. We check if the low number of resolution elements in our data affects our measurements, since the velocity dispersion calculated might vary by more than 20 per cent if sufficient number of pixels are not available to resolve the clump. To investigate whether we have enough pixels to be operating in the saturated regime (where velocity dispersion does not change by more than 20 per cent when the number of resolution elements are altered), we perform a resolution degradation on clump A by creating artificial 'superpixels' (merging nearby pixels to make a bigger pixel) and then applying the gradient fit and subtraction algorithm.

For the first degradation (1/4 resolution), we merge four nearby pixels into one (making a square shape, see Fig. 5). While the centre of a superpixel is the centroid of the four constituent pixels, its CO (5–4) velocity is the flux-weighted average of CO (5–4) velocities in the constituent pixels:

$$v_{spix} = \left(\frac{\sum_{i=1}^{4}(S_i\, v_i)}{\sum_{i=1}^{4} S_i} \right), \tag{6}$$

where v_{spix} is the velocity of the superpixel, S_i is the flux of the ith constituent pixel, and v_i is its velocity. At places where pixels belonging to the clump A cannot make a square by themselves, we use pixels from outside the clump, but mask their flux to be 0. Thus, for such constituent pixels, $S_i = 0$, so these pixels do not contribute to the sums in equation (6).
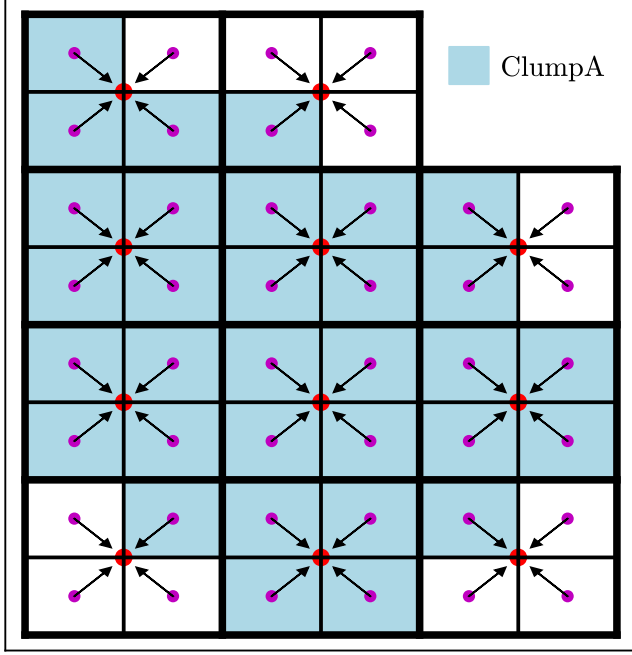
Figure 5. First resolution degradation through creation of 11 superpixels, by merging nearby pixels using a flux-weighted averaging method (see equation 6). Thick lines denote the boundaries of superpixels whereas thinner lines denote the boundaries of pixels. Red dots depict the centre of superpixels and purple dots depict the centre of pixels. Pixels belonging to clump A are shown in blue; they are the same as those shown in Fig. 3. Pixels outside the clump are shown in white. Arrows show the movement of a pixel when it is merged with other pixels to create a superpixel.
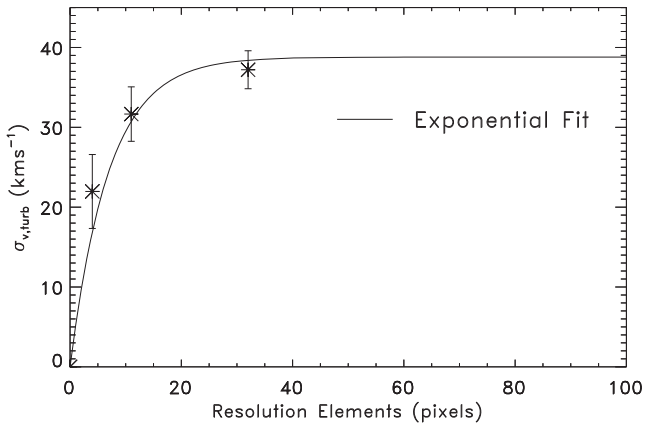
Figure 6. Turbulent velocity dispersion at different resolutions, fitted with a growing exponential function of the form $A_0 (1 - e^{-N/N_0})$, where N is the number of resolution elements. $N_0 \sim 7$ for the best-fitting model, which implies the velocity dispersion does not change by more than 5 per cent for $N \gtrsim 20$.

We do this process twice: decreasing the resolution to (1/4) and (1/16) of the original resolution. This results in a total of 11 and 4 superpixels after the first and second resolution degradation, respectively. Fig. 6 shows the turbulent velocity dispersions we get at the three resolutions. We fit a growing exponential of the form $A_0 (1 - e^{-N/N_0})$ (where N is the number of resolution elements) to this data. Since decreasing the resolution by (1/4) does not alter the velocity dispersion by $\gtrsim 20$ per cent (as we notice from Fig. 6),

we confirm that we have enough pixels to resolve this clump with acceptable accuracy.

5 GAS MASS AND FREEFALL TIME FROM CO (5–4)

The total gas mass is an essential parameter which goes in all the star formation relations we test in a later section (see Section 6). It can be estimated by following the CO (1–0) emission in the star-forming region (Carilli & Blain 2002; Pety et al. 2013; McNamara et al. 2014; Scoville et al. 2017). From fig. 1 in Rybak et al. (2015b), and that in Dye et al. (2015), we notice that there is a significant presence of CO (1–0) emission at the position of clump A. However, the CO (1–0) data was obtained by the Karl G. Jansky Very Large Array (Valtchanov et al. 2011) at a lower resolution than ALMA and cannot be used for kinematic analysis. Thus, we rely on ALMA observations of CO (5–4) transition (observed at a frequency of 142.57 GHz in ALMA band 4), to estimate the gas mass of clump A. It should be noted that CO (5–4) is generally a poor tracer of the total diffuse molecular gas, but is bright and easily observable at high redshift (Daddi et al. 2015; Lu et al. 2015; Yang et al. 2017).

We follow the Solomon, Radford & Downes (1992a); Solomon, Downes & Radford (1992b) relation between line luminosity and integrated flux density of CO (5–4):

$$L'_{CO(5-4)} = 3.25 \times 10^7 \, S_v \, \Delta v \, \frac{D_L^2}{v_{obs}^2 (1+z)^3}, \tag{7}$$

where $L'_{CO(5-4)}$ is the line luminosity in K km s^{-1} pc^2, $S_v \Delta v$ is the velocity integrated flux density of CO (5–4) after subtraction of background emission, in Jy km s^{-1}, D_L is the luminosity distance in Mpc, and v_{obs} is the observed frequency of transition in GHz. The line luminosity we obtain is $L'_{CO(5-4)} = (5.04 \pm 1.10) \times 10^8$ K km s^{-1} pc^2. Since the transition we observe with ALMA at $z \approx 3$ is higher than the ground (1–0) transition, we introduce an appropriate line ratio factor (defined as the ratio of line luminosity of CO (5–4) to that of CO (1–0)), $r_{54} = 0.28 \pm 0.05$. This value was derived for clump A by S15, where the authors used velocity and magnification maps from the lens model prepared by Dye et al. (2015). It falls in the typical range of values of r_{54} for SMGs (see Carilli & Walter (2013) and references therein).

To get the gas mass from the line luminosity, we use an appropriate CO to H$_2$ conversion factor α_{CO}. Although there is a high uncertainty in the value of this factor for nearby as well as high-redshift galaxies (Narayanan et al. 2012; Papadopoulos et al. 2012), the suggested values based on observations of SMGs lie in the range ~ 0.8–1.0 M$_\odot$ per (K km s^{-1} pc^2) (Downes & Solomon 1998; Solomon & Vanden Bout 2005; Tacconi et al. 2008; Magdis et al. 2011; Hodge et al. 2012; Bolatto, Wolfire & Leroy 2013; Bothwell et al. 2013; Carilli & Walter 2013), which is less by a factor of ~ 4 than the typical value used for Milky Way clouds and nearby galaxies. Dye et al. (2015) used a conversion factor of unity (in the same units) for SDP 81, while Hatsukade et al. (2015) used a value of 0.8. Further, we notice that clump A falls on top of the starburst sequence of the Σ_{gas}–Σ_{SFR} relation populated by local ultra-luminous infrared galaxies and SMGs (Daddi et al. 2010). This further justifies the choice of $\alpha_{CO} \sim 0.8$–1 M$_\odot$ per (K km s^{-1} pc^2).

Keeping these studies in mind, we assume $\alpha_{CO} \approx 0.9 \pm 0.2$ M$_\odot$ per (K km s^{-1} pc^2), which gives an H$_2$ mass of

$(4.5 \pm 1.0) \times 10^8 \, \mathrm{M_\odot}$.[1] Accounting for the contribution to the gas by He, we further increase the H_2 mass obtained so far by 36 per cent to get the total gas mass for clump A as $(6.2 \pm 1.4) \times 10^8 \, \mathrm{M_\odot}$. This value is in good agreement with the gas mass found out using SED fitting in Section 3. The gas surface density we derive is $\Sigma_{gas} = (8.6 \pm 1.9) \times 10^9 \, \mathrm{M_\odot \, kpc^{-2}}$, where we calculate and sum the area of all pixels which constitute clump A.[2] The size of clump A we obtain in this manner is $R \sim 0.15 \pm 0.02 \, \mathrm{kpc}$, in excellent agreement with the size we find through composite disc profile fitting in Section 3.1. Assuming clump A to be spherical (see Section 4 for a discussion on the validity of this assumption), we calculate its density to be $\rho = M_{gas}/V = (2.9 \pm 0.6) \times 10^{-21} \, \mathrm{g \, cm^{-3}}$, where V is the volume of the spherical clump.

To establish whether the cloud is undergoing collapse, we estimate the virial parameter α_{vir}, which is the ratio of twice the kinetic energy to the gravitational energy (Federrath & Klessen 2012). Using the definition from Bertoldi & McKee (1992), the virial parameter can also be given by

$$\alpha_{vir} = \frac{5\sigma_{v,tot}^2}{4\pi G R^2 \rho}, \tag{8}$$

where the velocity dispersion σ_{tot} is the total thermal and turbulent velocity dispersion including the shear component (i.e. turbulent velocity dispersion before gradient subtraction, $\sigma_{v,bgs}$). However, in this clump, since the turbulent velocity dispersion $\sigma_{v,bgs} \gg c_s$, it implies that the total velocity dispersion can be approximated as $\sigma_{v,tot} \approx \sigma_{v,bgs}$ (Krumholz & McKee 2005; Federrath & Klessen 2012). The virial parameter we thus obtain is $\alpha_{vir} = 0.63 \pm 0.13 < 1$, implying the cloud is strongly gravitationally bound and likely undergoing collapse. For such a cloud, the freefall time can be given by (Hennebelle & Chabrier 2011, 2013; Chabrier, Hennebelle & Charlot 2014):

$$t_{ff} = \sqrt{\frac{3\pi}{32 G \rho}}, \tag{9}$$

where G is the gravitational constant. From this equation, we obtain a freefall time of $1.3 \pm 0.1 \, \mathrm{Myr}$. This value is in agreement with freefall times calculated for other high z starbursts (see table 4 of Krumholz, Dekel & McKee 2013).

We summarize all the parameters going into predictions of SFR surface density in various star formation relations in Table 1.

6 COMPARISON OF OBSERVED SFR SURFACE DENSITY WITH THEORETICAL PREDICTIONS BY K98, KDM12, AND SFK15

We compare the SFR surface density obtained through dust SED fitting with star formation relations proposed for nearby and high-redshift galaxies in Fig. 7. The PDF of the measured SFR surface density in clump A is shown as the solid line, and we compare it with the predictions of SFR surface density by three popular star formation relations in the same plot. These PDFs were calculated using MC simulations with a sample size of 100 000 and included systematic errors on the SFR surface densities.

---

[1]This gas mass is essentially in agreement as that obtained by S15 for clump A. However, due to a typographical error, the gas masses reported in the last column of table 1 of S15 have to be rearranged. For the 5 clumps, the reported gas masses are in the order D-C-A-B-E.
[2]The size of 1 pixel is ~0.05 kpc. There are 32 pixels in this clump.
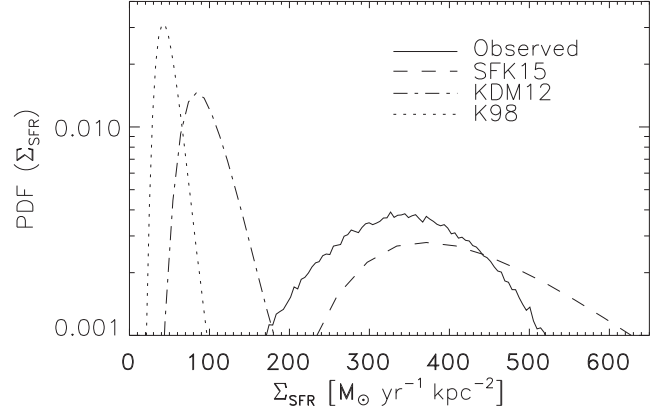
Figure 7. PDF of Σ_{SFR} estimated from dust SED fitting (solid curve) and those predicted from K98 (dotted curve, equation 10), KDM12 (dot–dashed curve, equation 11) and SFK15 (dashed curve, equation 12) relations. The PDFs were calculated using MC simulations with a sample size of 100 000.

The Kennicutt–Schmidt (KS or K98) relation is given by (Schmidt 1959; Kennicutt 1998b):

$$\Sigma_{SFR} = 2.53 \times 10^{-4} \, \Sigma_{gas}^{1.4 \pm 0.15}, \tag{10}$$

The distribution of SFR surface density (Σ_{SFR}) we obtain using equation (10) is shown as the dotted line in Fig. 7. The mean SFR surface density we calculate from the KS relation is $\Sigma_{SFR} = 84 \pm 27 \, \mathrm{M_\odot \, yr^{-1} \, kpc^{-2}}$. Since equation (10) is based on the Salpeter IMF, we correct the SFR surface density for a Chabrier IMF (similar to that done in Section 3) and obtain $\Sigma_{SFR} = 52 \pm 17 \, \mathrm{M_\odot \, yr^{-1} \, kpc^{-2}}$.[3] We find that the KS relation underestimates the SFR surface density by a factor $\gtrsim 3.3$, with respect to the observed SFR surface density in this clump, even when the 1σ uncertainty is taken into account. Numerous studies have discussed the breakdown of the KS relation on the scales of ~100 pc in local (Onodera et al. 2010; Shi et al. 2011; Becerra & Escala 2014; Xu et al. 2015) and high-redshift environments (Bouché et al. 2007; Daddi et al. 2010; Genzel et al. 2010).

Krumholz, Dekel, and McKee (KDM12) showed that the SFR does not only depend on gas surface density but also on the depletion time of the gas under collapse. Their single-freefall time model takes the form:

$$\Sigma_{SFR} = f_{H_2} \epsilon_{ff} \frac{\Sigma_{gas}}{t_{ff}}, \tag{11}$$

where f_{H_2} is the fraction of gas available in molecular form (assumed to be unity), and ϵ_{ff} is the SFR per freefall time. They found a best-fitting $\epsilon_{ff} = 0.015$ (see Krumholz et al. 2013). The freefall time they used is the minimum of the Toomre time-scale (equation 8 in KDM12) and the giant molecular cloud (GMC) freefall time (equation 4 in KDM12). The SFR surface density suggested from KDM12 is $\Sigma_{SFR} = 106 \pm 37 \, \mathrm{M_\odot \, yr^{-1} \, kpc^{-2}}$. We plot the PDF of the predicted SFR surface density from KDM12 as the dot–dashed line in Fig. 7.

As can be seen from Fig. 7, both KS and KDM12 relations underestimate the observed SFR surface density in clump A. In order to match the SFR surface density predicted by the KS or KDM12

---

[3]This distribution does not take into account the uncertainty on the power-law index in equation (10) because we notice that it becomes highly skewed when this uncertainty is randomized. In that case, the 16th and 84th percentile values of Σ_{SFR} are 1 and $133 \, \mathrm{M_\odot \, yr^{-1} \, kpc^{-2}}$, respectively.

relations with that observed, the dust temperature (which goes into the MBB function, see equation 1) should be lowered by ∼8 K, if emissivity is fixed at the best-fitting emissivity $\beta_{em} = 2.5$. Another way could be to decrease the emissivity to 1.9 such that the original best-fitting temperature ($T = 39$ K) can provide a reasonable match of observed SFR surface density with that predicted by KS or KDM12 relations. Although these values of (T, β_{em}) are not favoured by the SED fit, they are in the typical range of dust temperature and emissivity found out for other high-redshift galaxies (Smith et al. 2013; Ota et al. 2014; Lu et al. 2015, 2017). Furthermore, in order to fit the KS relation to the observed SFR surface density in this clump, we find that the power law should be steeper with an exponent of $n \approx 1.6$ in equation 10). This is consistent with scaling in the KS relation estimated for other SMG galaxies and starbursts (Bouché et al. 2007; Khoperskov & Vasiliev 2017). Moreover, Daddi et al. (2010) also proposed that the KS relation underpredicts the star formation efficiency in starburst galaxies by a factor of 10. Similarly, an equivalence between observed SFR surface density and that predicted by KDM12 relation can be obtained if ϵ_{ff} in equation (11) is increased to thrice its best-fitting value. These discrepancies between observed and predicted SFR surface density motivate us to include the role of turbulence in star formation relations, as suggested by SFK15.

The SFK15 relation is the result of the combination of gas surface density and density-dependent freefall time determined by KDM12 (see also Krumholz et al. 2013) and the role of turbulence in star-forming regions (Federrath & Klessen 2012; Federrath 2013). SFK15 correlated the scatter present in the KDM12 relation with turbulent motions in gas clouds and found that Σ_{SFR} is ∼0.45 per cent of the multi-freefall gas consumption rate (MGCR) in star-forming regions:

$$\Sigma_{SFR} = \left(\frac{0.45}{100}\right) \frac{\Sigma_{gas}}{t_{ff}} \left(1 + b^2 \mathcal{M}^2 \frac{\beta_{mag}}{\beta_{mag} + 1}\right)^{3/8}, \quad (12)$$

where b is the turbulent driving parameter ($b = 1/3$ for solenoidal driving and $b = 1$ for compressive driving) (Federrath, Klessen & Schmidt 2008; Federrath et al. 2010; Federrath & Klessen 2012; Federrath 2013). We use a mixed driving mode with $b = 0.4$ (Federrath et al. 2010). The turbulence term was derived by Molina et al. (2012). In this term, β_{mag} is the ratio of thermal to magnetic pressure. It can also be expressed as a ratio of Alfvén to sonic Mach numbers: $\beta_{mag} = 2 \mathcal{M}_A^2 / \mathcal{M}^2$. The freefall time used in this equation comes from min ($t_{ff,T}$, $t_{ff,GMC}$), where T stands for Toomre and GMC stands for giant molecular clouds, as used by KDM12. KDM12 showed that the Toomre time is shorter than the GMC freefall time for starburst galaxies. We do not have any estimates of magnetic field strength in this galaxy since it requires polarization or Zeeman measurements of the magnetic field, which are unavailable for SDP 81. For simplicity, we neglect magnetic fields and set $\beta_{mag} \to \infty$, leading to $\beta_{mag}/(\beta_{mag} + 1) = 1$.

The SFK15 relation (equation 12) generates a skewed distribution of predicted SFR surface density, as shown in Fig. 7. The mean of the distribution is $\Sigma_{SFR} = 491^{+139}_{-194}$ M$_\odot$ yr^{-1} kpc^{-2}, where the errors represent the 16th and 84th percentiles. As can be seen from Fig. 7, the distribution of SFR surface density predicted from SFK15 overlaps to a good extent with the distribution of the observed SFR surface density. The overestimation of SFR surface density by SFK15 can be attributed to ignoring the magnetic field strength, which can reduce the SFR by a factor of ∼2 (Padoan & Nordlund 2011; Federrath & Klessen 2012; Federrath 2015).

Fig. 8 depicts the observed SFR surface density (Σ_{SFR}) plotted against the gas surface density (Σ_{gas}) and single and multi-freefall

times, overlayed with the three star formation relations, consistent with the Chabrier IMF. We also plot other star formation relations based on gas surface density [Bigiel et al. 2008 (B08); Heiderman et al. 2010 (H10); Wu et al. 2010 (W10), and Bigiel et al. 2011 (B11)] in the first panel of Fig. 8. While the H10 relation can possibly explain the observed SFR surface density in the clump A in SDP 81, it is not universally applicable. Other star formation relations shown in this panel cannot account for observed SFR surface density in all the molecular clouds. Additionally, we also note that SDP 81 lies on one of the dashed lines in the middle panel of Fig. 8, which represent deviations by a factor of 3 from the best-fitting relation of KDM12 (shown as the solid line). It is evident that there is a large scatter in both the K98 and KDM12 relations, which we calculate from

$$\chi^2_{red} = \frac{1}{N_D} \sum \left(\frac{\Sigma_{SFR}\,(observed) - \Sigma_{SFR}\,(predicted)}{E}\right)^2, \quad (13)$$

where E is the measured error on Σ_{SFR} (observed) and N_D is the number of star-forming regions.[4] We emphasize that we do not fit any relations to compute the scatter but simply perform a χ^2 minimization routine. From equation (13), we calculate a reduced χ^2 scatter of $\chi^2_{red} = 50.1$ and 7.27 for the KS and KDM12 relations, respectively. The final panel in Fig. 8 illustrates the turbulence-based SFK15 relation. We observe that the characteristics of the clump A in SDP 81 match the SFK15 relation to a good extent. The scatter we obtain for the SFK15 relation is 1.25. It has significantly reduced as compared to the scatter from KS and KDM12 relations because the SFK15 relation includes systematic variations in the Mach number, as were established by Federrath (2013). This highlights the role of turbulence in star-forming regions (Federrath & Klessen 2012; Kraljic et al. 2014). The validity of the multi-freefall star formation relation has been previously supported in an independent work by Braun & Schmidt (2015).

7 CONCLUSIONS

Using high-resolution (sub-kpc) ALMA data of SDP 81 – a high-redshift ($z\sim 3$) lensed galaxy, we have measured the SFR surface density in its biggest and most isotropic clump, revealed by the lensing analysis of Dye et al. (2015). Through dust SED fitting with an MBB spectrum for this clump (clump A in S15), we find the best-fitting dust temperature to be T = 39 ± 2 K when an emissivity index β_{em}= 2.5 is used . Taking into account the systematic errors resulting from partially cold temperature dominated flux and assuming that this clump has conditions similar to those in the whole galaxy, we obtain the SFR surface density in this clump as $\Sigma_{SFR} = 357^{+135}_{-85}$ M$_\odot$ yr^{-1} kpc^{-2}.

Using CO (5–4) flux and velocity data for this galaxy, we obtain a turbulent velocity dispersion of $\sigma_{v,\,turb} = 37 \pm 5$ km s^{-1}, corresponding to a turbulent Mach number $\mathcal{M} = 96 \pm 28$. This is higher than the typical Mach numbers found for local galaxies, but is in agreement with those estimated for high-redshift starbursts. The turbulent velocity dispersion that goes into estimating this Mach number is obtained from the large-scale gradient subtraction of CO (5–4) velocity in the plane of the sky, which is in good agreement with the velocity dispersion obtained along the line of sight by S15 after correcting for beam smearing. Using an appropriate CO

---

[4]For the calculation of scatter, only those data are included for which Σ_{SFR} (predicted) is available for each of K98, KDM12, and SFK15 relations.
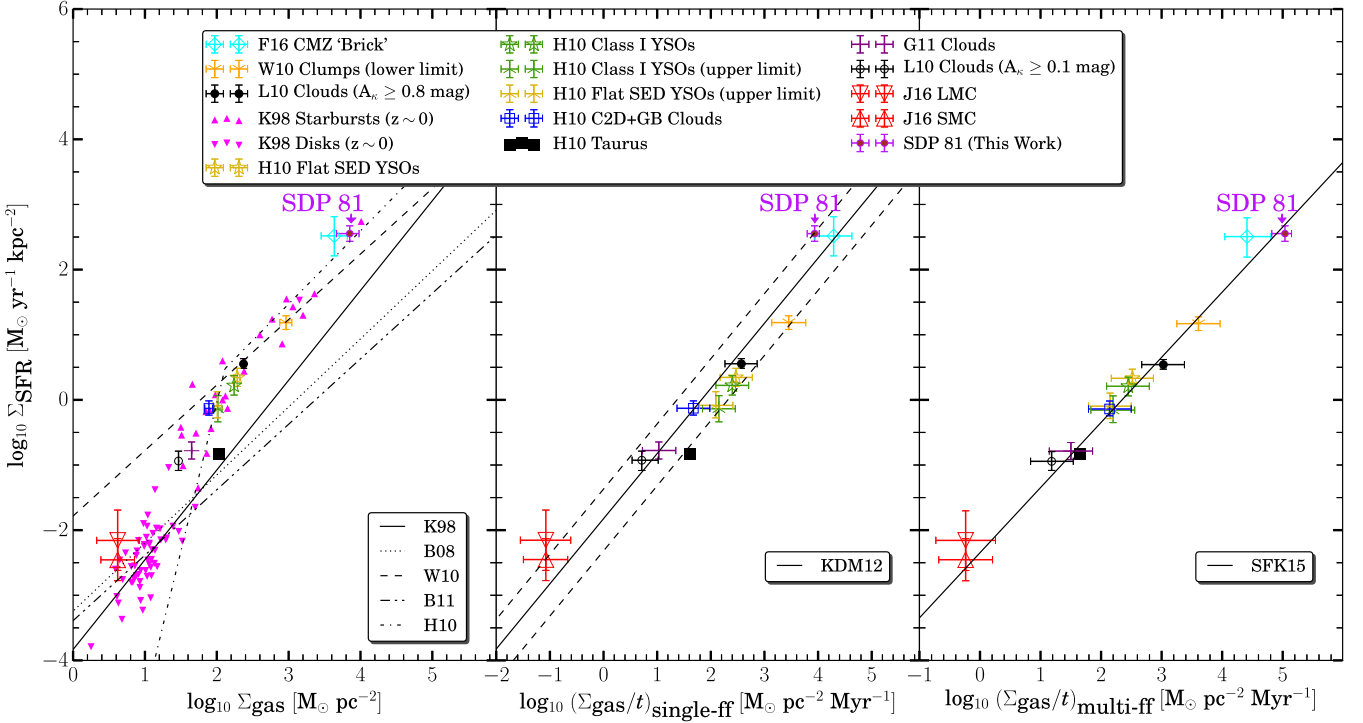
Figure 8. *Left-hand panel:* Observations of $\Sigma_{\rm SFR}$ (SFR surface density) in local clouds, plotted against gas surface density. The data is extracted from Heiderman et al. (2010, H10), Lada, Lombardi & Alves (2010, L10), Wu et al. (2010, W10), Gutermuth et al. (2011, G11), and Jameson et al. (2016, J16). Data for the Brick molecular cloud in the CMZ is taken from Federrath et al. (2016, F16). The K98 (discs and starbursts) data were adjusted in KDM12, Krumholz et al. (2013), and Federrath (2013) to the Chabrier IMF, similar to that done for the high-redshift data by Daddi et al. (2010). The systematic difference between starbursts and the original K98 relation is due to different $\alpha_{\rm CO}$ conversion factors used for starbursts and discs (see section 2 of Daddi et al. 2010 and fig. 1 of Federrath 2013). SFR relations proposed by Kennicutt (1998b, K98) (corrected for Chabrier IMF), Bigiel et al. (2008, B08), Bigiel et al. (2011, B11), Wu et al. (2010, W10), and Heiderman et al. (2010, H10) are also shown. *Middle panel:* Observations of $\Sigma_{\rm SFR}$ plotted against the single-freefall time. Solid line depicts the best-fitting model from KDM12, with $\epsilon_{\rm ff} = 0.015$ (see Krumholz et al. 2013); dashed lines illustrate deviations by a factor of 3 from the best fit. *Right-hand panel:* Observations of $\Sigma_{\rm SFR}$ plotted against the turbulence-based multifreefall model proposed by Salim et al. (2015, SFK15). Solid line represents equation (12). Clump A analysed in this work is marked with an arrow in all the three panels. The scatter obtained through a χ^2 minimization routine for K98, KDM12, and SFK15 relations is 50.1, 7.27, and 1.25, respectively.

to H_2 conversion factor for this galaxy, we find the gas mass in the clump we study to be $(6.2 \pm 1.4) \times 10^8\,{\rm M_\odot}$, which is in agreement with that found out using the best-fitting MBB by using a typical gas to dust ratio of 150.

On testing star-forming relations based on gas mass, freefall times and turbulence (available in literature), we find that the KS relation underpredicts the observed SFR surface density in this clump ($\Sigma_{\rm SFR, KS} = 52 \pm 17\,{\rm M_\odot\,yr^{-1}\,kpc^{-2}}$) by a factor $\gtrsim 3.3$, which can be corrected for if the dust temperature is lowered while keeping the emissivity same or vice versa. It is also clear that the other star formation relations as plotted in first panel of Fig.8 are not universally applicable. Further, the single-freefall time based KDM12 relation also underestimates the observed SFR surface density in this clump, giving $\Sigma_{\rm SFR, KDM} = 106 \pm 37\,{\rm M_\odot\,yr^{-1}\,kpc^{-2}}$; however, it can explain the observed SFR if deviations up to a factor of 3 from its best-fitting model are considered. We also find that the large scatter present in these star formation relations can be explained by turbulence acting in this clump. The turbulence regulated multi-freefall model by SFK15 predicts the SFR surface density as $\Sigma_{\rm SFR, SFK} = 491^{+139}_{-194}\,{\rm M_\odot\,yr^{-1}\,kpc^{-2}}$. The overestimation of SFR surface density by SFK15 can be attributed to ignoring magnetic fields while calculating the SFR through equation (12). Our findings emphasize the role of turbulence giving rise to the multifreefall model of the SFR and its consistency with the observed SFR in molecular clouds in local as well as high-redshift galaxies.

ACKNOWLEDGEMENTS

REFERENCES

Aceves H., Velázquez H., Cruz F., 2006, MNRAS, 373, 632
ALMA Partnership, 2015, ApJ, 808, L4
Battersby C., Bally J., Dunham M., Ginsburg A., Longmore S., Darling J., 2014, ApJ, 786, 116
Becerra F., Escala A., 2014, ApJ, 786, 56
Bertoldi F., McKee C. F., 1992, ApJ, 395, 140
Bigiel F., Leroy A., Walter F., Brinks E., de Blok W. J. G., Madore B., Thornley M. D., 2008, AJ, 136, 2846
Bigiel F. et al., 2011, ApJ, 730, L13
Blain A. W., Barnard V. E., Chapman S. C., 2003, MNRAS, 338, 733
Blanc G. A., Heiderman A., Gebhardt K., Evans N. J., II, Adams J., 2009, ApJ, 704, 842
Bolatto A. D., Wolfire M., Leroy A. K., 2013, ARA&A, 51, 207
Bothwell M. S. et al., 2013, MNRAS, 429, 3047
Bouché N. et al., 2007, ApJ, 671, 303
Bournaud F. et al., 2014, ApJ, 780, 57
Bradač M. et al., 2017, ApJ, 836, L2
Braun H., Schmidt W., 2015, MNRAS, 454, 1545
Brisbin D. et al., 2017, A&A, 608, A15
Bussmann R. S. et al., 2013, ApJ, 779, 25
Caon N., Capaccioli M., D'Onofrio M., 1993, MNRAS, 265, 1013
Carilli C. L., Blain A. W., 2002, ApJ, 569, 605
Carilli C. L., Walter F., 2013, ARA&A, 51, 105
Casey C. M., 2012, MNRAS, 425, 3094
Cañameras R. et al., 2017, A&A, 604, A117
Chabrier G., 2003, ApJ, 586, L133
Chabrier G., Hennebelle P., Charlot S., 2014, ApJ, 796, 75
Chang Y.-Y., van der Wel A., da Cunha E., Rix H.-W., 2015, ApJS, 219, 8
Cibinel A. et al., 2017, MNRAS, 469, 4683
Ciotti L., Bertin G., 1999, A&A, 352, 447
Coppin K. et al., 2008, MNRAS, 384, 1597
Cowie L. L., Hu E. M., Songaila A., 1995, AJ, 110, 1576
Cresci G. et al., 2009, ApJ, 697, 115
Da Cunha E., Eminian C., Charlot S., Blaizot J., 2010a, MNRAS, 403, 1894
Da Cunha E., Charmandaris V., Díaz-Santos T., Armus L., Marshall J. A., Elbaz D., 2010b, A&A, 523, A78
Daddi E. et al., 2010, ApJ, 714, L118
Daddi E. et al., 2015, A&A, 577, A46
Danielson A. L. R. et al., 2017, ApJ, 840, 78
Decarli R. et al., 2016, ApJ, 833, 70
Downes D., Solomon P. M., 1998, ApJ, 507, 615
Draine B. T., Lee H. M., 1984, ApJ, 285, 89
Dunne L., Eales S., Edmunds M., Ivison R., Alexander P., Clements D. L., 2000, MNRAS, 315, 115
Dye S. et al., 2014, MNRAS, 440, 2013
Dye S. et al., 2015, MNRAS, 452, 2258
Elmegreen B. G., 2002, ApJ, 577, 206
Elmegreen B. G., 2015, ApJ, 814, L30
Elmegreen B. G., Hunter D. A., 2015, ApJ, 805, 145
Elmegreen B. G., Scalo J., 2004, ARA&A, 42, 211
Elmegreen D. M., Elmegreen B. G., Marcus M. T., Shahinyan K., Yau A., Petersen M., 2009, ApJ, 701, 306
Escala A., 2015, ApJ, 804, 54
Falgarone E. et al., 2017, Nature, 548, 430
Federrath C., 2013, MNRAS, 436, 3167
Federrath C., 2015, MNRAS, 450, 4035
Federrath C., Klessen R. S., 2012, ApJ, 761, 156
Federrath C., Klessen R. S., Schmidt W., 2008, ApJ, 688, L79

Federrath C., Roman-Duval J., Klessen R. S., Schmidt W., Mac Low M.-M., 2010, A&A, 512, A81
Federrath C. et al., 2016, ApJ, 832, 143
Freundlich J. et al., 2013, A&A, 553, A130
Fudamoto Y. et al., 2017, MNRAS, 472, 2028
Förster Schreiber N. M. et al., 2009, ApJ, 706, 1364
Gao Y., Solomon P. M., 2004, ApJ, 606, 271
Genzel R. et al., 2006, Nature, 442, 786
Genzel R. et al., 2010, MNRAS, 407, 2091
Griffin M. J. et al., 2010, A&A, 518, L3
Guo K., Zheng X. Z., Wang T., Fu H., 2015, ApJ, 808, L49
Gutermuth R. A., Pipher J. L., Megeath S. T., Myers P. C., Allen L. E., Allen T. S., 2011, ApJ, 739, 84
Hatsukade B., Tamura Y., Iono D., Matsuda Y., Hayashi M., Oguri M., 2015, PASJ, 67, 93
Hayward C. C., Kereš D., Jonsson P., Narayanan D., Cox T. J., Hernquist L., 2011, ApJ, 743, 159
Heiderman A., Evans N. J., II, Allen L. E., Huard T., Heyer M., 2010, ApJ, 723, 1019
Hennebelle P., Chabrier G., 2011, ApJ, 743, L29
Hennebelle P., Chabrier G., 2013, ApJ, 770, 150
Hennebelle P., Falgarone E., 2012, A&AR, 20, 55
Hezaveh Y. D. et al., 2013, ApJ, 767, 132
Hezaveh Y. D. et al., 2016, ApJ, 823, 37
Hildebrand R. H., 1983, QJRAS, 24, 267
Hodge J. A., Carilli C. L., Walter F., de Blok W. J. G., Riechers D., Daddi E., Lentati L., 2012, ApJ, 760, 11
Hodge J. A. et al., 2016, ApJ, 833, 103
Hogg D. W., Baldry I. K., Blanton M. R., Eisenstein D. J., 2002, preprint (arxiv.org/abs/astro-ph/0210394)
Humason M. L., Mayall N. U., Sandage A. R., 1956, AJ, 61, 97
Ikarashi S. et al., 2015, ApJ, 810, 133
Immer K., Kauffmann J., Pillai T., Ginsburg A., Menten K. M., 2016, A&A, 595, A94
Inoue K. T., Minezaki T., Matsushita S., Chiba M., 2016, MNRAS, 457, 2936
Jameson K. E. et al., 2016, ApJ, 825, 12
Johnson S., Wilson G., Tang Y. AzTEC Team 2013, in American Astronomical Society Meeting Abstracts #221. p. 431.03
Johnson T. L. et al., 2017, ApJ, 843, L21
Kauffmann J., Bertoldi F., Bourke T. L., Evans N. J., II, Lee C. W., 2008, A&A, 487, 993
Kennicutt R. C., Evans N. J., 2012, ARA&A, 50, 531
Kennicutt R. C., , Jr, 1998a, ARA&A, 36, 189
Kennicutt R. C., , Jr, 1998b, ApJ, 498, 541
Khoperskov S. A., Vasiliev E. O., 2017, MNRAS, 468, 920
Klessen R. S., 2000, ApJ, 535, 869
Kovács A., Chapman S. C., Dowell C. D., Blain A. W., Ivison R. J., Smail I., Phillips T. G., 2006, ApJ, 650, 592
Kraljic K., Renaud F., Bournaud F., Combes F., Elmegreen B., Emsellem E., Teyssier R., 2014, ApJ, 784, 112
Krieger N. et al., 2017, ApJ, 850, 77
Krumholz M. R., McKee C. F., 2005, ApJ, 630, 250
Krumholz M. R., Dekel A., McKee C. F., 2012, ApJ, 745, 69
Krumholz M. R., Dekel A., McKee C. F., 2013, ApJ, 779, 89
Lada C. J., Lombardi M., Alves J. F., 2010, ApJ, 724, 687
Laporte N. et al., 2017, ApJ, 837, L21
Lehmann E., Casella G., 1998, Theory of Point Estimation. Springer-Verlag, Berlin
Li A., Draine B. T., 2001, ApJ, 554, 778
Lu N. et al., 2015, ApJ, 802, L11
Lu N. et al., 2017, ApJ, 842, L16
Mac Low M.-M., Klessen R. S., 2004, Rev. Mod. Phys., 76, 125
Madau P., Dickinson M., 2014, ARA&A, 52, 415
Magdis G. E. et al., 2011, ApJ, 740, L15
Magdis G. E. et al., 2012, ApJ, 760, 6
McKee C. F., Ostriker E. C., 2007, ARA&A, 45, 565

McMullin J. P., Waters B., Schiebel D., Young W., Golap K., 2007, in Shaw R. A., Hill F., Bell D. J., eds, ASP Conf. Ser. Vol. 376, Astronomical Data Analysis Software and Systems XVI. Astron. Soc. Pac., San Francisco. p. 127

McNamara B. R. et al., 2014, ApJ, 785, 44

Miettinen O., Delvecchio I., Smolčić V., Aravena M., Brisbin D., Karim A., 2017, A&A, 602, L9

Molina F. Z., Glover S. C. O., Federrath C., Klessen R. S., 2012, MNRAS, 423, 2680

Narayanan D., Krumholz M. R., Ostriker E. C., Hernquist L., 2012, MNRAS, 421, 3127

Negrello M. et al., 2010, Science, 330, 800

Negrello M. et al., 2014, MNRAS, 440, 1999

Nguyen-Luong Q. et al., 2016, ApJ, 833, 23

Nightingale J. W., Dye S., 2015, MNRAS, 452, 2940

Ogilvie J., 1984, Comput. Chem., 8, 205

Oke J. B., Sandage A., 1968, ApJ, 154, 21

Onodera S. et al., 2010, ApJ, 722, L127

Ota K. et al., 2014, ApJ, 792, 34

Padoan P., Nordlund Å., 2011, ApJ, 730, 40

Papadopoulos P. P., van der Werf P. P., Xilouris E. M., Isaak K. G., Gao Y., Mühle S., 2012, MNRAS, 426, 2601

Paulino-Afonso A. et al., 2018, MNRAS, 476, 5479

Pety J. et al., 2013, ApJ, 779, 43

Renaud F., Kraljic K., Bournaud F., 2012, ApJ, 760, L16

Rybak M., McKean J. P., Vegetti S., Andreani P., White S. D. M., 2015a, MNRAS, 451, L40

Rybak M., Vegetti S., McKean J. P., Andreani P., White S. D. M., 2015b, MNRAS, 453, L26

Salim D. M., Federrath C., Kewley L. J., 2015, ApJ, 806, L36

Salpeter E. E., 1955, ApJ, 121, 161

Sargent M. T. et al., 2014, ApJ, 793, 19

Schmidt M., 1959, ApJ, 129, 243

Schreiber C. et al., 2015, A&A, 575, A74

Scoville N. et al., 2017, ApJ, 836, 66

Sersic J. L., 1968, Atlas de Galaxias Australes. Observatorio Astronomico, Cordoba, Argentina

Shapiro K. L., Genzel R., Förster Schreiber N. M., 2010, MNRAS, 403, L36

Shi Y., Helou G., Yan L., Armus L., Wu Y., Papovich C., Stierwalt S., 2011, ApJ, 733, 87

Silk J., 1997, ApJ, 481, 703

Simpson J. M. et al., 2015, ApJ, 799, 81

Smail I., Ivison R. J., Blain A. W., 1997, ApJ, 490, L5

Smail I., Ivison R. J., Blain A. W., Kneib J.-P., 2002, MNRAS, 331, 495

Smith D. J. B. et al., 2013, MNRAS, 436, 2435

Solomon P. M., Radford S. J. E., Downes D., 1992a, Nature, 356, 318

Solomon P. M., Downes D., Radford S. J. E., 1992b, ApJ, 398, L29

Solomon P. M., Vanden Bout P. A., 2005, ARA&A, 43, 677

Speagle J. S., Steinhardt C. L., Capak P. L., Silverman J. D., 2014, ApJS, 214, 15

Spilker J. S. et al., 2016, ApJ, 826, 112

Springel V., Hernquist L., 2003, MNRAS, 339, 312

Swinbank A. M. et al., 2015, ApJ, 806, 5

Tacconi L. J. et al., 2008, ApJ, 680, 246

Tacconi L. J. et al., 2010, Nature, 463, 781

Tamura Y., Oguri M., Iono D., Hatsukade B., Matsuda Y., Hayashi M., 2015, PASJ, 67, 72

Trujillo I., Graham A. W., Caon N., 2001, MNRAS, 326, 869

Valtchanov I. et al., 2011, MNRAS, 415, 3473

Van den Bergh S., Abraham R. G., Ellis R. S., Tanvir N. R., Santiago B. X., Glazebrook K. G., 1996, AJ, 112, 359

Warren S. J., Dye S., 2003, ApJ, 590, 673

Wong T., Blitz L., 2002, ApJ, 569, 157

Wong K. C., Suyu S. H., Matsushita S., 2015, ApJ, 811, 115

Wong K. C., Ishida T., Tamura Y., Suyu S. H., Oguri M., Matsushita S., 2017, ApJ, 843, L35

Wright E. L., 2006, PASP, 118, 1711

Wu J., Evans N. J., II Gao Y., Solomon P. M., Shirley Y. L., Vanden Bout P. A., 2005, ApJ, 635, L173

Wu J., Evans N. J., II, Shirley Y. L., Knez C., 2010, ApJS, 188, 313

Xu C. K. et al., 2015, ApJ, 799, 11

Yang C. et al., 2017, A&A, 608, A144

Zanella A. et al., 2015, Nature, 521, 54

This paper has been typeset from a TEX/LATEX file prepared by the author.